Superconductivity in Films of Pb/PbSe Core/Shell Nanocrystals

Pavlo Zolotavin and Philippe Guyot-Sionnest*

James Franck Institute, The University of Chicago, 929 E. 57th Street, Chicago, Illinois 60637, United States

ABSTRACT

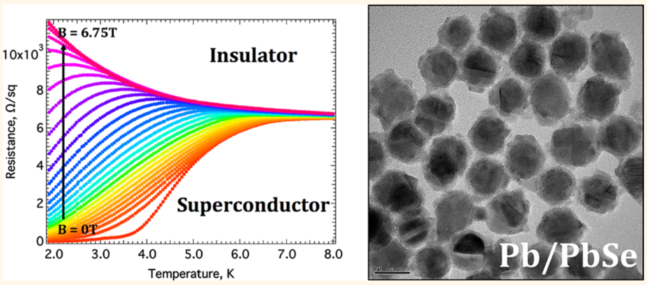

Superconductivity in films of electronically coupled colloidal lead nanocrystals is reported. The coupling between particles is *in situ* controlled through the conversion of the oxides present on the surface of the nanoparticles to chalcogenides. This transformation allows for a 10^9-fold increase in the conductivity. The temperature of the onset of the superconductivity was found to depend upon the degree of coupling of the nanoparticles in the vicinity of the insulator—superconductor transition. The critical current density of the best sample of Pb/PbSe nanocrystals at zero magnetic field was determined to be 4×10^3 A/cm^2. In turn, the critical field of the sample shows 50-fold enhancement compared to bulk Pb.

KEYWORDS: superconductivity · granular film · superconductor—insulator transition · critical current · magnetoresistance · transition temperature · monodisperse · metal nanoparticles · Pb · PbSe · colloidal · core—shell

Colloidal nanocrystals offer ample opportunities for the design of novel composite materials that are inaccessible with a top-down approach. Superconductivity generates perpetual fundamental interest and has promising practical applications; however colloidal nanoparticles of superconducting metals receive little attention from the nanoscale community. In the future, one could expect to use nanostructuring to improve the critical parameters of superconductors (SC) by fine-tuning the electronic properties of the composite material. The simplest starting point for such a material would be a film of colloidal nanocrystals. The basic question that then arises is what are the sufficient conditions for such a film of nanoparticles to become a SC. This question was studied over the last several decades both theoretically and experimentally.[1,2] The central parameter that defines the physical properties of a granular array is the average tunneling conductance between neighboring grains g expressed in units of $4e^2/h$ ($g^{-1} = 6.45$ kΩ).

In the low coupling limit, when $g \ll 1$, the emergence of the SC requires that the electrostatic charging energy, E_C, of the nanocrystals should be smaller than the Josephson coupling energy, E_J, between adjacent crystals. For two SC separated by a tunneling barrier, E_J is given by the Ambegaokar—Baratoff expression, $E_J = \pi g \Delta \tanh(\Delta/2KT)$, where Δ is the temperature- and magnetic field-dependent SC gap.[3]

When the coupling is increased, the charging energy decreases through the renormalization due to virtual electron tunneling processes, and when $g > 1$, the charging energy becomes $E_C = \Delta/g$ and is always smaller than E_J.[4] Therefore the transition to the SC state occurs when g is 1 or larger, implying that the macroscopic SC is observed when the sheet resistance of the film is $R_Q = 6.45$ kΩ or less. When the material is insulating in its normal state, which means that the resistance increases with lowering the temperature, there can be a superconductor—insulator (S—I) transition driven by the disorder, decreased coupling between particles, or simply magnetic field.[1]

Prior experiments in this field were carried out with films prepared by gas condensation methods,[5,6] using disordered materials such as InO_X and TiN[7−9] or using arrays of Josephson junctions (JJA) prepared by lithography.[10−12] They have provided a good testing ground for theories, but they lack the scalability, the size control, and the chemical versatility that can potentially be obtained with the assembly of colloidal nanocrystals.

We previously developed a synthesis of colloidal Pb nanoparticles, and Meissner effect studies showed that the uncoupled nanocrystals, when larger than 11.7 nm, become SC with critical temperature (T_C)

* Address correspondence to pgs@uchicago.edu.

Received for review June 19, 2012 and accepted July 19, 2012.

10.1021/nn302709d

close to that of the bulk Pb.[13] In this article, we report low-temperature transport measurements in films of electronically coupled nanocrystals. To increase the coupling between particles, the oxide present on the surface of the particles is converted to chalcogenides (−S, −Se, −Te), therefore creating lead/lead chalcogenide core/shell nanocrystals. Varying the extent of the conversion or the chalcogenides enables the gradual transformation from insulating to superconducting behavior. We also studied the magnetoresistance of the films up to 9 T and measured the critical current.

RESULTS AND DISCUSSION

Sample. The nanocrystals consist of a lead core and an amorphous oxide shell, which protects the particles from further oxidation and is a mixture of PbO and SnO.[13] For the purpose of simplicity, we will refer to the shell as being PbO in the following text. Films of nanocrystals can be prepared following several established procedures.[14−16] The large size of the lead crystals limits the solubility in hexane, which prevented the use of the standard hexane−octane route for film formation.[17] The Pb nanoparticles self-assembled in an ordered monolayer array at the surface of diethylene glycol,[18] but this method requires long drying periods after each layer deposition. In this work, we developed a variation of the drop-casting method for film preparation from a toluene solution. The details of this procedure are given in the Methods section. This procedure leads to uniformly disordered films in the center of the substrate, where the digits of the electrodes are located.

The long organic ligands on the surface of the crystal and the oxide shell prevent electrical conductivity. Even after ligand removal using hexamethyldisilane, the films still show a resistance larger than 10^{11} Ω/sq. The chemical transformation of the oxide shell to the corresponding chalcogenides[19] provides an avenue for increased coupling. When metal oxides are exposed to a reactive source of a chalcogenide, the chalcogenide can easily substitute for the oxygen. A simple example of this process is $PbO_{(s)} + H_2S_{(g)} \rightarrow PbS_{(s)} + H_2O_{(g)}$, which is thermodynamically spontaneous under standard conditions. Here we report results for conversion of the oxide to sulfide and selenide. While it is possible to perform the oxide to telluride transformation, PbTe is itself superconducting when deficient in either Pb or Te, with $T_C \approx 5.2$ K.[20] On the other hand, PbS, SnS, PbSe, and SnSe are not superconducting by themself or in combination, therefore providing a cleaner experimental system of superconducting particles imbedded in the insulating matrix.

A typical result of the PbO to PbS conversion is shown in Figure 1B. After an exposure to hydrogen sulfide, the particles show a crystalline shell with a lattice spacing corresponding to PbS. A detailed report of the shell formation is beyond the scope of this article, but several interesting features are noted. In contrast to the amorphous PbO shell, the transformation to the crystalline sulfide shell disrupts the original spherical shape of the crystal, producing multiple facets. There is only a 2% lattice mismatch between the (200) planes of PbS and (111) planes of Pb, which results in locally coherent interfaces. The PbS shell has a larger thickness than the PbO shell. The shell thickness is increased for higher substrate temperatures and longer exposure times, as shown in Figure S2, and at sufficiently high temperatures the whole particle is converted to PbS. The shell growth is accompanied by a reduction in core diameter, which suggests partial conversion of the core Pb metal to PbS. This is consistent with the inward diffusion of the sulfur atoms and outward diffusion of the metal ions. Compared with PbO the molar volume of PbS is 35% larger. This leads to the expansion of the shell and filling of the voids between crystals. In some cases, there is a fusion of the shells from neighboring nanocrystals. This in turn increases the area of contact between particles and should facilitate the tunneling between the crystals. There is also a variation of the shell thickness between the individual facets, and this might reflect that different crystallographic directions have different diffusion rates. For nanocrystals with diameters less than 13 nm, the PbS shell is typically of nonuniform thickness around the particle, leaving one or two facets with a very thin shell. For larger crystals, the shell covers the surface of the crystal rather uniformly.

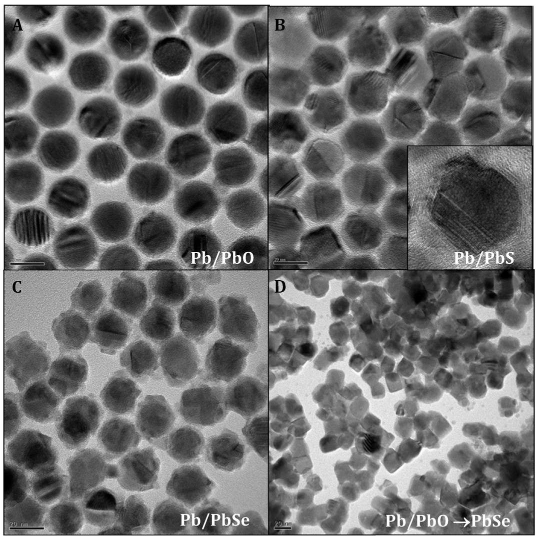

Figure 1. (A) Typical Pb nanocrystals with a core diameter of 20 ± 1 nm and shell thickness of 1.6 nm. (B) Particles after the oxide shell is converted to PbS. Inset is a picture of one of the crystals. (C) Nanocrystals after the shell is converted to PbSe. (D) PbSe nanocrystals after being overexposed to $(tms)_2Se$ at 155 °C. All scale bars are 20 nm.

When using bis(trimethylsilyl)selenide, $(tms)_2Se$, as the reactive source of selenium, the chalcogenide shell

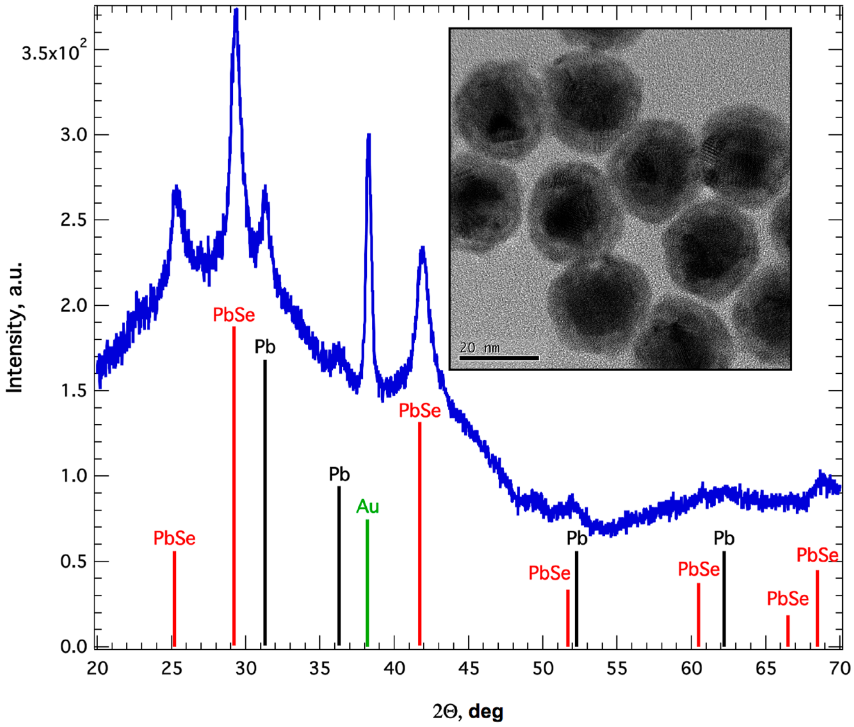

Figure 2. XRD and TEM (inset) of the *in situ* transformed particles. The core of 20 ± 1 nm particles is reduced to 16 ± 2 nm after transformation. The width of the PbSe peaks corresponds to a particle size of 13 nm, which is in fair agreement with 10 nm expected from TEM images. The peak marked as Au is due to the gold electrodes used to make transport measurements.

consists of 2–5 nm PbSe granules instead of 9–13 nm wide epitaxial facets as was observed for the PbS shell. Figure 1C shows an example of the PbO to PbSe shell transformation. Figure 1D shows particles that were completely converted to PbSe at a higher substrate temperature becoming cubic in the process. With selenization, the decrease in the core diameter is less pronounced and the shell roughness is larger compared with the case of the sulfurization from H_2S. The outward shell growth may be due to the enrichment of the PbSe in selenium due to the additional thermal decomposition of $(tms)_2Se$ on the surface of the nanocrystals. It was observed that, when switching from H_2S to $(tms)_2S$, the PbS shell structure also becomes less faceted and more granular, as shown in Figure S3. There are other differences between $(tms)_2S$ and H_2S that point to a lower reactivity of the former. When a toluene solution of $(tms)_2S$ is used as the ligand-removing agent at room temperature, we do not observe shell transformation nor a decrease in the resistance of the film. However bubbling H_2S, also at room temperature, through the colloidal solution of Pb nanocrystals results in the precipitation and formation of the crystalline PbS shell, Figure S4. Even when ligands are present in excess, the precipitation is rapid. These observations suggest that if one would use H_2Se as a selenium source, higher crystallinity shells might be expected. Due to the difficulties in synthesizing dry H_2Se gas, we did not corroborate this hypothesis, and this will be a subject for future experiments.

Transferring the sample back and forth between the PPMS and the vacuum chamber for increased exposures did not work satisfactorily. To address this limitation, we opted for an *in situ* transformation. A sample and a container containing the selenium precursor were enclosed together in an airtight cell inside the cryostat. A gradual decrease in resistance is obtained by briefly heating to 107 °C before a low-temperature measurement cycle. With a given sample, this *in situ* transformation allows the observation of the evolution of the *R*(*T*) curves over a range of normal-state resistance. The X-ray diffraction (XRD) spectrum and transmission electron microscope (TEM) images taken after the last cycle are used to confirm the presence of the metallic core, as shown Figure 2. We note however that we were not able to transform samples all the way from the fully insulating original oxide shell to a SC state with zero resistance, because the *in situ* transformation reaches saturation. Therefore, we used a first exposure in the vacuum chamber to achieve a resistance of an intermediate value and then used *in situ* transformation to decrease the resistance stepwise until the SC state was reached.

In any chemical transformation of a nanoparticle solid, "necking" is a distinct possibility. As judged by TEM images of films with high and low conductivity, no significant morphological changes could be observed in the structure of the film during the shell conversion. If the metallic cores were to form a percolative path of metallic conductivity, one would see a sudden transition to metallic behavior. However, the resistance changes continuously during the transformation. Furthermore, the samples discussed in the text are all insulators in their normal state.

TEM images of nanocrystals presented here show the transformation that occurs in one monolayer thick films; however transport experiments were performed on 6–9 layer thick films. Gaseous reactants can efficiently penetrate films of nanocrystals, as known with atomic layer deposition.[21] However, the real picture is more complicated and requires extra discussion. XRD spectra of thick films subjected to the conditions of $(tms)_2Se$ exposure and temperature identical with those of the samples on the TEM grid, which appeared fully converted, Figure 1D, still showed the presence of crystalline lead, Figure S5. This suggests that for high temperatures or prolonged exposures the top layer of the film may be completely converted to lead chalcogenide, whereas the bottom of the film preserves some core/shell structure. It is possible that after the initial uniform conversion the diameter of the pores between nanocrystals decreases due to the shell expansion. Thermal decomposition of the selenium precursor would also contribute to the premature pore closing of the top layer of the film. This results in an inhomogeneous interparticle coupling between individual layers and smaller core diameters of the top layer. We emphasize that this occurs only to overexposed films, and this leads to very distinct effects in the $R(T)$ dependence. This will lead to a different critical temperature of the top surface. As a result, the temperature dependence of the resistance develops an inhomogeneous section or a peak close to the transition temperature. This was observed for some samples such as shown in Figure S6. Similar artifacts were reported in high-T_C materials when copper oxide planes have different critical temperature due to the nonuniform oxygenation.[22−24] The artifacts discussed above were not frequently observed; however they may create issues in future applications of the Pb/PbSe nanocrystals.

Transport. Lead oxide has a direct band gap of ∼3.2 eV,[25] which leads to a high resistance of the untreated films. An estimate of the tunneling resistance between adjacent nanocrystals is the sheet resistance of the film. As was mentioned before, it is greater than 10^{11} Ω/sq for the Pb/PbO films. When the oxide is substituted by the chalcogenide, the band gap is reduced more than 10 times, which vastly lowers the tunneling resistance. The large reduction of resistance upon shell conversion is partially reversible, as the resistance of the film increases by 4–5 orders of magnitude after a brief exposure to air. The Pb/PbS samples had larger sheet resistance than the Pb/PbSe (PbS has a larger band gap than PbSe) and never showed zero resistance SC at temperatures accessible by the experimental setup. In the rest of paper we focus on the results for Pb/PbSe nanocrystals.

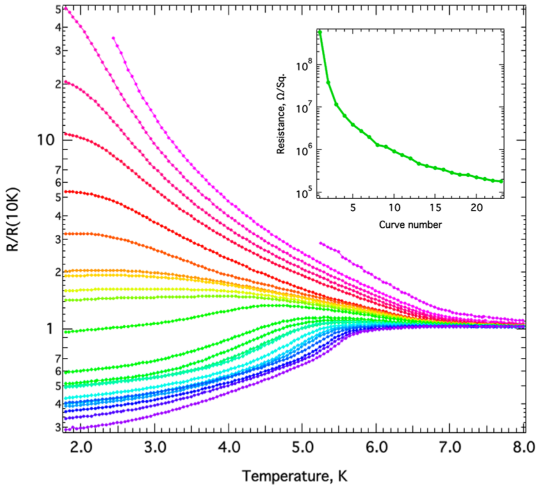

Figure 3. Temperature dependence of the resistance for an *in situ* transformed film. Higher resistance curves correspond to the smaller degree of conversion. Curves are numbered from the top to the bottom. Data in the temperature range from 1.8 to 250 K are shown in Figure S8. Inset: sheet resistance as a function of curve number.

Non-SC Samples. Figure 3 shows a series of $R(T)$ curves for only *in situ* transformed Pb/PbSe nanocrystals for which a nonzero resistance is still observed at the lowest achievable temperature of 1.8 K. Each curve is normalized by the value of resistance at $T = 10$ K. The top curve corresponds to the first temperature cycle, when the sample had the largest resistance. The resistance of the film is progressively reduced at each cycle from 5×10^8 Ω/sq to 10^5 Ω/sq, as shown by the inset. For the first three curves, the resistance actually increases exponentially below the superconducting transition of the individual particles at $T_{C0} \approx 6.9$ K. When the sheet resistance of the film is reduced further (red curves), there is a deviation from the exponential growth. Starting with curve #7 (orange), there is a peak in the resistance at some temperature T^*, which marks the onset of the SC transition. T^* increases for subsequent exposure to $(tms)_2Se$, finally reaching 7.05 K, as shown in the inset of Figure 4. At this point the resistance decays monotonically below T_{C0}, but the T_C of the sample remains still beyond the accessible temperature range. For this data set $g \ll 1$, and it can be discussed in terms of the charging energy and the Josephson energy.

The charging energy of a single nanocrystal in the array of metallic particles is estimated by $E_C = (s/(d/2 + s))(e^2/\varepsilon d)$, where d is the diameter of the particles, s is the spacing between particles, and e is elementary charge.[26,27] This is based on the capacitance of the metal sphere embedded in a metallic shell, with an insulating gap of thickness s.[28] For a particle with $d = 16$ nm and $s = 4$ nm in a matrix of organic ligands with $\varepsilon \approx 2.2$, the charging energy is 230 K.

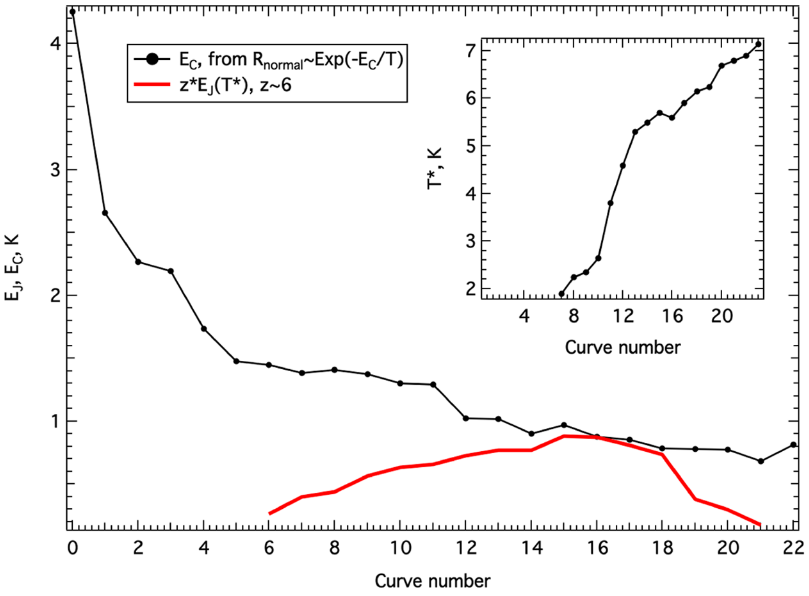

Figure 4. Charging energy and Josephson energy at *T plotted for data from Figure 3. Inset: *T** plotted *versus* curve number.**

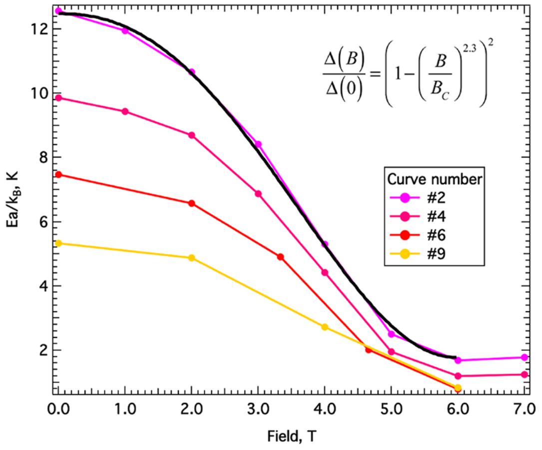

Figure 5. Activation energy as a function of magnetic field. E_A was fitted in the linear part of the ln $R(1/T)$ curves. Curve numbers correspond to the curves in Figure 3. The black curve is a fit to the field dependence of the SC gap,[12] giving $B_C = 6 \pm 1$ T.

The large dielectric constant of the PbSe shell, ε_{PbSe} = 210, drastically reduces this energy to 2.3 K.[39] The charging energy is determined from the $R \approx \exp(E_C/T)$ fit to the normal-state temperature dependence above T_{C0}, and it agrees well with the estimate above, Figure 4.

Curves #1–5. Below T_{C0} a SC gap opens in the individual particles. For curve #2 the sample is in the low-coupling limit with $g \simeq 2 \times 10^{-4}$ and $E_{J,T=0} \approx z\pi g\Delta \approx 60$ mK, where z is a coordination number.[29,30] This is much smaller than $E_C \approx 2.5 \pm 0.1$ K. In this situation, Cooper pairs cannot tunnel and transport is carried out by quasiparticles that are thermally excited over the SC energy gap. Below T_{C0}, the activation energy is then $E_A \approx E_C + \Delta$. When the SC gap is suppressed by a magnetic field, the activation energy drops back to the same activation energy as the one above T_{C0} with $E_A \approx E_C$, Figure 5. This regime of transport was observed before in granular SCs,[31−34] disordered SCs,[9] and in JJA.[12] In some experiments the variable range hopping law $R \approx \exp((T'/T)^{1/2})$ was used to fit the temperature dependence in the insulating regime; however a nearest neighbor hopping provides a better fit to the data in our case.[35] When fitted by $R \approx \exp((E_C + \Delta)/T)$, we obtain $\Delta = 10.0 \pm 0.1$ K, which is smaller than $\Delta_{0,20\mathrm{nm}\ \ \mathrm{Pb}} = 14.6$ K.[13] Close to T_{C0}, the $R(T)$ curves in Figure 3 deviate from the exponential behavior because of the gap temperature dependence. However fitting data with the standard $\Delta(T)$ equation suggested a temperature dependence that is sharper than usual. A direct measurement of $\Delta(T)$ by tunneling conductance could elucidate this disagreement in the future.

As shown in Figure 6, Δ is decreased when the magnetic field or the coupling is increased. Fitting the data for curve #2 with a power law resulted in a critical field of 6 T, which agrees well with the value obtained from the Meissner effect.[13] The decrease of E_A as the coupling increases is expected, since we approach the SC state and the probability of the Cooper pair tunneling should increase; however we did not find a theory to quantitatively describe this transformation.

There are alternative descriptions to the simple Coulomb blockade picture discussed above. It has been suggested that the exponential resistance is instead due to the emergence of a dynamic Coulomb barrier, Δ_C.[36] This description was later challenged, and we also do not find agreement with this theoretical treatment.[37] When applied to the data in Figure 3, this theory underestimates the activation barrier by a factor of 3.

Another suggestion is that transport in the insulating state of granular SC occurs *via* variable range

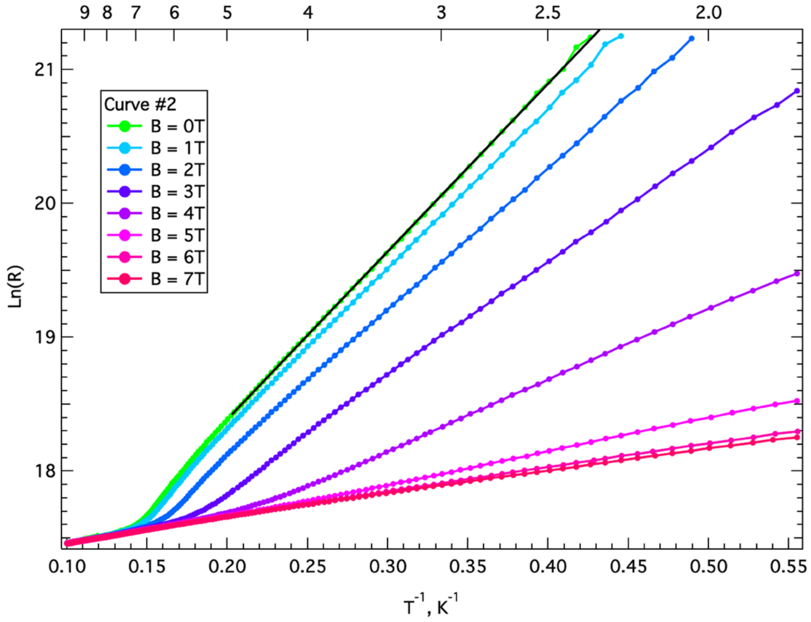

Figure 6. Data for the second curve from Figure 3. Resistance as a function of temperature for different magnetic fields.

hopping. If $E_C > \Delta$, it is predicted to occur through single electron hopping. If $E_C < \Delta$, it would be Cooper pair hopping.[38] In this case, the magnetoresistance (MR) should be positive, since increased magnetic field would destroy the Cooper pairs and increase the resistance. For the data shown in Figure 3, the condition $E_C < \Delta$ is satisfied; however the MR is negative.

Curves #6–22. According to several possible phase diagrams of granular SC, we can expect a macroscopic SC state with zero resistance when either $g \ll 1$ and $E_C < E_J$ (Anderson–Abeles criterion) or $g \geq 1$ regardless of E_C/E_J ratio.[2,4,39] For JJA it was shown that for arrays with $E_C < E_J$ lower than 1.7, macroscopic SC could be established.[11] We can, therefore, expect that when $E_C \approx E_J$, the onset of SC behavior should be observed for a sample with $g < 1$. When the PbO shell is converted to PbSe, the shell effective dielectric constant is continuously reduced and E_C decreases, while E_J is increasing as the conductance of the film continues to grow. We speculate that when E_C is on the order of $E_J(T)$, the Josephson channel should open. This lowers the resistance and indicates the onset of the SC transition. Figure 4 shows the extracted values of E_C and E_J from the $R(T)$ curves in Figure 3. E_C is taken from the measured normal part of the $R(T)$ curve, and E_J is calculated using the Ambegaokar–Baratoff expression[3] at T^*. As T^* approaches T_{C0}, $E_J(T^*)$ first increases as g grows, reaches a maximum for curve #16, and then starts to decrease due to the decrease of the magnitude of the SC gap when approaching T_{C0}. Figure 4 shows that indeed there is a correlation between the onset of the SC, T^*, and the point where $E_C \approx E_J$, providing a qualitative support for the argument developed above. It is difficult to develop a more quantitative discussion based on the scaling[40] or theory developed for JJA arrays,[41] because the temperature range does not allow reaching T_C. We believe that the qualitative argument is quite good at this stage.

Previous studies on granular Pb deposited from the gas phase show results broadly similar to those obtained here.[42] However, Gerber reported a "flattening" of the $R(T)$ dependence at low temperatures for several depositions followed by a sudden switch to the fully SC state with a $T_C \approx 4$ K for one additional deposition. Instead, in the colloidal Pb, by gradually increasing the coupling between the Pb cores, there is a detailed evolution of the $R(T)$ curves displaying a smooth transition from insulating to the SC state without reentrant behavior.

The SC contribution to conductivity below T^* is easily destroyed by the magnetic field, as seen in Figure S7. For curve #11 from Figure 3, the additional conductivity from SC fluctuations below $T^* = 3.8$ K is suppressed by a magnetic field of 2 T. The film again shows insulating behavior with thermally activated transport. The 10% reduction of the SC gap, as estimated from the shift of T_{C0}, is not sufficient to significantly change E_J compared to E_C. If the change in the SC gap was the reason for the large positive MR below T^*, then the temperature dependence in the field of 2 T for curve #11 is similar to curve #10 in zero field; however this is not the case. In the low coupling limit, T_C can be estimated as $T_C = (z/4)E_J$,[2] which yields $T_C \approx 0.16$ K for the sample in Figure S7. The fluctuation-induced decrease in the resistance below T^* is therefore observed far from T_C, and large sensitivity of the fluctuation corrections to the magnetic field may explain the positive MR.[43–45]

SC Samples. To achieve a macroscopic SC, the samples are first partially converted to Pb/PbSe using the vacuum conversion method before starting the *in situ* transformation. Data are shown in Figure 7. For the first curve, #0, the normal state resistance is far above R_Q and the film may show a transition to the SC state but with T_C beyond the available temperature range. Therefore, data in Figure 7 can be viewed as the continuation of the evolution shown in Figure 3. Curves #1 to #4 show the transition to the SC state. The first two curves have a normal state resistance slightly above R_Q. The transition temperature increases as the normal-state resistance decreases; however it quickly reaches saturation. The initial drop in resistance can be approximately fitted with the Halperin–Nelson expression, $R_{SQ} \approx \exp(-\mathrm{const}/(T - T'_C)^{1/2})$, which applies for the Berezinsky–Kosterlitz–Thouless (BKT)-type transition in thin SC films.[46] Another signature of the BKT transition is the sign change of the $R(B)$ curvature at $B = 0$.[8] This is observed at temperatures close to T_C, Figure S9. The essence of the BKT transition is that at T_C vortices form bound pairs and stop propagating through the sample. This phenomenon was observed in disordered systems[8,47] and granular metals.[6] The motion of vortex–antivortex pairs induces voltages across the film, which is manifested by a finite resistance in the SC state. Similarly to previously reported data on granular tin,[6] the $R(T)$ dependence departs from the BKT expression to a thermally activated behavior, $R \approx \exp(-E'_A/T)$. In Figure 7 this is seen as the Arrhenius part at low temperatures. The activation energy E'_A is attributed to vortex motion and is related to the pinning potential that prevents vortices from propagating. The efficient vortex motion due to poor pinning should be mirrored in the low magnitude of the critical current, J_C. Indeed, values of J_C in the best sample of Pb/PbSe nanocrystals are ~10^4 times smaller when compared to the bulk Pb, Figure 8. A similar performance was observed for granular aluminum,[48] when the size of the particles became smaller than the effective coherence length. For the JJA, the energy barrier for vortex propagation was shown to be

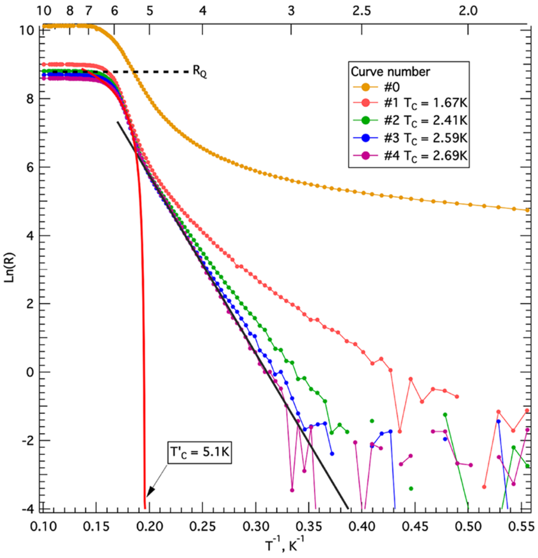

Figure 7. Transformation to fully SC state. The red line shows the BKT fitting of the initial decrease of resistance. The black line is a linear fit in the region of thermally activated motion of vortices. The horizontal dashed line shows the value of R_Q. Data in the temperature range from 1.8 to 300 K are shown in Figure S13.

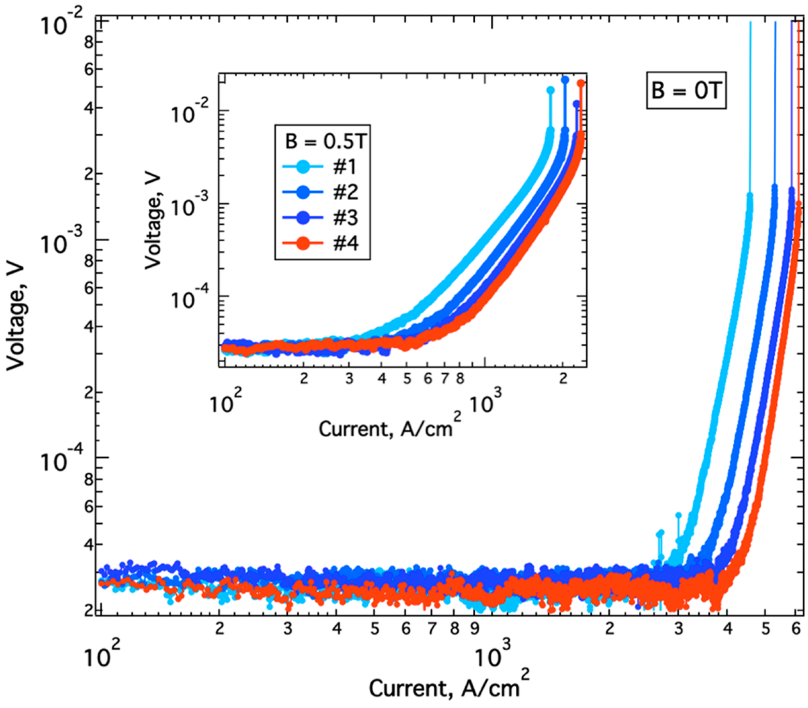

Figure 8. I–V curves at zero field for the increasing degree of transformation. $J_{C,\mathrm{Bulk}} \approx 5 \times 10^7$ A/cm^2. Inset: Film maintains supercurrent at $B = 0.5$ T, while $H_{C,\mathrm{Bulk}} = 0.08$ T.

proportional to E_J.[49] The latter depends inversely on the normal-state resistance, and therefore E'_A should increase from curve #1 to #4, as indeed seen in Figure 7.

The thermally activated motion of vortices should dominate when the flux-flow resistance of the free vortices is larger than the resistance from the motion of vortex−antivortex pairs.[6] The free vortices could originate from a stray magnetic field that is inevitably present in the laboratory. When estimated from the conditions above, the equivalent field that would create the observed flux-flow resistance is 25 mT. Such a large field is unlikely to be present in the cryostat. Also, this would imply a sharp MR peak close to this field at temperatures close to the T_C, which is not observed. Therefore there should be another, more efficient, source for vortex excitation. One possibility is that the vortices are introduced due to the noise in the measuring leads, which were not filtered with low pass filters used in other experiments.[6,11,12]

The MR of the SC samples shows a pronounced peak at high field, before the sample turns normal, Figure S10. This behavior is typical for disordered and granular systems.[7,9,34] The relative amplitude of this peak decreases as the coupling between the dots is increased, as was observed earlier.[7] It was initially argued that this peak is due to the SC fluctuations.[44] Recently this suggestion was developed, and a complete solution for the fluctuation-induced corrections to conductance was obtained.[45] As a simple experimental estimate we report the value of the field at which the resistance is half of its normal value.[7] For example, for curve #2 from Figure 7 the critical field at 2 K was 4.2 T. This number is more than 50 times larger than the bulk lead critical field of 0.08 T.

Using the Ginzburg−Landau expression for the critical field $H_{C2} = \Phi_0/2\pi\xi^2$, we can estimate the corresponding coherence length to be 28 nm.[29] The coherence length in the dirty limit is $\xi_{\text{dirty}} = 0.85(\xi_0 l_{\text{eff}})^{1/2}$, where l_{eff} is the effective mean free path and ξ_0 is the coherence length of lead, which is 83 nm.[29] At low temperature l_{eff} should be comparable to the grain size, and therefore $\xi_{\text{dirty}} \approx 31$ nm, in agreement with the estimate from the value of H_{C2}.

When aproaching the S−I transition by increasing the conductivity, the transition should happen around $R = c_u R_Q$, where c_u is a constant close to unity and slightly differs depending on the theoretical formulation.[1] In Figure 7 two curves have normal-state resistances 1.25 and 1.05 times larger than R_Q, and the other two are smaller than R_Q; however all four show a SC transition. In Figure S11 another sample has a resistance slightly smaller than R_Q and shows a SC transition with $T_C = 1.5$ K. The large width of the sample might lead to the overestimation of the sheet resistance because thinner parts of the film might not turn SC and will be parallel to the SC parts. We estimate this error to be less than 15%; therefore within the experimental precision, our results agree with the theoretical expectation that the normal sheet resistance should be close to R_Q for observing a macroscopic SC state.

The transition temperature to the SC state is defined as the point when the resistance falls below our measuring threshold. In general, macroscopic SC should be confirmed by the measurements of thermodynamic properties such as magnetic susceptibility and heat capacity. The total volume of the SC material in the film is very small, which makes such experiments rather challenging. If the film has only local SC, there is a possibility that the film would become again insulating at some lower temperature. Such reentrant behavior was observed in only one sample when the thickness of the film was on the order of one monolayer throughout the entire width of the film between the electrodes. In this single case, the resistance started to rise at low temperature after an initial decrease by 2 orders of magnitude during the onset of SC, Figure S12. A reentrant behavior was previously observed in films of quench condensed metals.[5,42] In these literature examples, the amplitude of the resistance decrease during the onset of SC was never larger than one decade. In our experiments, however, the resistance decreases by more than 3 orders of magnitude before crossing the measurement floor. We believe that measurements of thermodynamic properties are not necessary and that, at present, there is enough data to claim the existence of macroscopic superconductivity in the films of Pb/PbSe nanocrystals.

An interesting question is whether the curves that show a decrease in resistance after T^* in Figure 3 could become SC at lower temperatures. The sheet resistance corresponding to these curves is signigificantly larger than R_Q, and a reentrant behavior at lower temperature may be expected. However, according to the Anderson−Abeles criterion, the sample at this level of interparticle coupling would become SC. In the experiment on films of oxidized metal particles, reentrant behavior was not observed down to 50 mK temperatures. It was also found that if the sample showed the onset of SC, it would eventually become SC at sufficiently low temperatures.[6] This suggests a speculative conclusion that these curves will reach zero resistance at sufficiently low temperatures. If this is indeed the case, then the separatrix between the insulator and superconductor phases will show unusually strong curvature, suggesting two-parameter scaling.[1] Future measurements at lower temperatures can clarify this issue.

CONCLUSION

In summary, the electrical transport and superconductivity of lead nanocrystal solids was studied. The material system was based on the assembly of colloidal lead nanocrystals that were insulated from one another by organic ligands and an oxide shell. The material described in this article is the first nanostructured superconductor prepared by the bottom-up approach starting from colloidal nanoparticles. The removal of the ligands followed by the controlled chemical transformation of the oxide shell to a chalcogenide shell with much lower barrier and higher dielectric constant allowed reducing the charging energy and increasing the Josephson energy. This provides control over the interparticle coupling, allowing one to observe the evolution of the system from insulating to superconducting. An unusual behavior of the *R*(*T*) dependence in the vicinity of the S−I transition was observed. The temperature of the SC onset was found to depend upon the degree of coupling of the nanoparticles. An argument based on the comparison of the charging energy and Josephson energy was developed to describe this observation. The magnetoresistance of the system in the magnetic fields up to 9 T was measured. It was found to agree with previous reports for similar systems and theoretical expectations for the bosonic mechanism of the S−I transition. The critical current density was determined to be 4×10^3 A/cm^2. One could anticipate the kinetic inductance to be greatly enhanced in a granular film compared to the bulk.[50] If the oxidation was prevented, high kinetic inductance could be useful for optical detection in the infrared and microwave regions. Future studies will focus on developing further the colloidal bottom-up assemblies and chemical processing aimed at designing better superconducting materials.

METHODS

Bis(trimethylsilyl)selenide, (tms)$_2$Se, was purchased from Gelest; lead stearate was purchased from Chem Service; all other materials were purchased from Sigma-Aldrich and used as received without purification. Solvents were of anhydrous grade, and all the procedures were made in a Schlenk line or in a glovebox with a nitrogen atmosphere. The sample transfer between the glovebox, cryostat, and a vacuum system for chemical transformation was performed in airtight containers under nitrogen.

Detailed procedures for the preparation and characterization of the lead nanocrystals were published previously.[13] A typical synthesis of the particles used in this work is the following. In 17 mL of 1-octadecene 240 mg of lead stearate, 4 mg of indium(III) acetylacetonate, and 0.1 mL of trioctylphosphine were dissolved. The reaction mixture was then degassed under vacuum for 30 min, periodically flushing the flask with argon. Under argon the temperature was increased to 244 °C, and 3.2 mL of a 0.06 M solution of bis[bis(trimethylsilyl)amino]tin(II) in hexadecane was rapidly injected. The temperature of the reaction mixture was stabilized at 216 °C and kept for 6 min, after which it was cooled to room temperature and transferred to the glovebox for cleaning. After several cleaning cycles, the particles were redissolved in toluene at a concentration of ~5 mg/mL. In the current work we used particles with a core diameter in the range 18−22 nm. All samples were monodisperse with a size distribution equal to 7% or better.

Gold electrodes for transport measurements in a four-probe configuration were prepared using standard UV lithography on a glass substrate. An example of the electrode layout is shown in Figure S1. A high length to width aspect ratio was necessary to allow measurement of highly resistive films. The copper wires were soldered to the electrode pads before the film deposition.

The films were prepared by drop-casting a solution of Pb nanocrystals on the surface of the electrodes, which were kept at 60 °C. A drop of the solution of particles covered the whole area of the substrate. When the surface of the substrate is flat, drying starts from the edges, leaving a circular ring pattern. However, the wires for transport measurements pin the liquid at the short edges of the substrate, forcing the toluene drop to start drying from the center. In the center of the substrate one can, therefore, obtain a rather uniform film. A thickness variation was less than or equal to 30% throughout the entire width of the film. The ligand removal was performed in two steps. After deposition, the films were immersed in the 1% solution of hydrazine in acetonitrile for 10 min, which prevents the nanocrystals from dissolving in toluene. The second step consists of submerging the film in the 1% solution of hexamethyldisilane in toluene for 10 min. The effectiveness of ligand removal was confirmed by the 90% reduction in the absorption of the C−H stretch band in the infrared spectra. To achieve a film of the necessary thickness, the deposition step followed by the ligand removal was repeated four times. Resulting film thicknesses were in the range 100 to 150 nm.

Transformation of the shell from oxide to chalcogenide was performed either in vacuum (~0.1 Torr) or in the airtight PPMS sample holder at atmospheric pressure inside the cryostat. During the conversion a film of particles was heated to 100−140 °C and exposed to vapors of (tms)$_2$Se or H_2S gas. The latter was used only in the low-pressure variant of the procedure. Both chemicals present a significant inhalation hazard and should be treated with utmost care. The resistance of the film was monitored *in situ*. To achieve the desired degree of transformation, the duration of the exposure to a chalcogenide precursor and the temperature of the films were varied. The optimal conditions for achieving low-resistance films were as follows: substrate temperature 135 °C for sulfur and 105 °C for selenium; exposure duration 5−7 min at a pressure of ~1 Torr.

The TEM images were obtained at 300 kV using an FEI Tecnai F30. For TEM characterization, dilute solutions of nanocrystals were drop-cast on the carbon-coated copper grids. Particles on the grid were subjected to the same procedures as a film on the electrodes. The diffraction patterns were collected using a Bruker D8 diffractometer with a Cu Kα X-ray source operating at 40 kV and 40 mA. The scanning electron images were obtained with an FEI NanoSEM 230. The thickness of the film was determined from the step height profile by a Veeco/Bruker NanoScope IIIA atomic force microscope in tapping mode.

The temperature- and field-dependent measurements were performed in the PPMS, Quantum Design. The sample(s), (tms)$_2$Se container, and TEM grid were enclosed in the custom-designed copper container. The resistance below 1 MΩ was measured using a built-in resistance bridge in the ac mode. The excitation current was limited to 10 μA. High-resistance samples were characterized by a Keithley 6517B in the two-probe configuration. Voltage−current curves were measured using Keithley 2612A source-measure unit in the pulsed mode to minimize heating. The threshold for voltage measurement was set to 10 mV.

Conflict of Interest: The authors declare no competing financial interest.

Acknowledgment. We thank Profs. I. S. Beloborodov, H. Jaeger, D. Shuster, and D. V. Talapin for fruitful discussions. The work was supported by the University of Chicago MRSEC NSF-DMR under Grant No. DMR-0213745.

Supporting Information Available: Additional material characterization data: electrode layout scheme, TEM and SEM images, XRD spectra, and shell thickness and core diameter for different conversion temperatures. Supplementary transport data: temperature and magnetic field dependence of the resistance for other samples and the magnetoresistance during the *in situ* conversion and near T_C. This material is available free of charge *via* the Internet at http://pubs.acs.org.

REFERENCES AND NOTES

1. Gantmakher, V. F.; Dolgopolov, V. T. Superconductor-Insulator Quantum Phase Transition. *Phys.-Usp.* **2010**, *53*, 1–49.
2. Beloborodov, I. S.; Lopatin, A. V.; Vinokur, V. M.; Efetov, K. B. Granular Electronic Systems. *Rev. Mod. Phys.* **2007**, *79*, 469–518.
3. Ambegaokar, V.; Baratoff, A. Tunneling between Superconductors. *Phys. Rev. Lett.* **1963**, *10*, 486–489.
4. Chakravarty, S.; Kivelson, S.; Zimanyi, G. T.; Halperin, B. I. Effect of Quasiparticle Tunneling on Quantum-Phase Fluctuations and the Onset of Superconductivity in Granular Films. *Phys. Rev. B* **1987**, *35*, 7256–7259.
5. Jaeger, H. M.; Haviland, D. B.; Orr, B. G.; Goldman, A. M. Onset of Superconductivity in Ultrathin Granular Metal Films. *Phys. Rev. B* **1989**, *40*, 182–196.
6. Watanabe, M.; Shimada, H.; Kobayashi, S.; Ootuka, Y. Superconductor-Insulator Transition in Granular Films of Tin. *J. Phys. Soc. Jpn.* **1997**, *66*, 1419–1426.
7. Steiner, M.; Kapitulnik, A. Superconductivity in the Insulating Phase above the Field-Tuned Superconductor-Insulator Transition in Disordered Indium Oxide Films. *Phys. C (Amsterdam, Neth.)* **2005**, *422*, 16–26.
8. Baturina, T. I.; Postolova, S. V.; Mironov, A. Y.; Glatz, A.; Baklanov, M. R.; Vinokur, V. M. Superconducting Phase Transitions in Ultrathin Tin Films. *Europhys. Lett.* **2012**, *97*, 17012.
9. Sambandamurthy, G.; Engel, L. W.; Johansson, A.; Shahar, D. Superconductivity-Related Insulating Behavior. *Phys. Rev. Lett.* **2004**, *92*, 107005.
10. Takahide, Y.; Yagi, R.; Kanda, A.; Ootuka, Y.; Kobayashi, S.-i. Superconductor-Insulator Transition in a Two-Dimensional Array of Resistively Shunted Small Josephson Junctions. *Phys. Rev. Lett.* **2000**, *85*, 1974–1977.
11. van der Zant, H. S. J.; Elion, W. J.; Geerligs, L. J.; Mooij, J. E. Quantum Phase Transitions in Two Dimensions: Experiments in Josephson-Junction Arrays. *Phys. Rev. B* **1996**, *54*, 10081–10093.
12. Delsing, P.; Chen, C. D.; Haviland, D. B.; Harada, Y.; Claeson, T. Charge Solitons and Quantum Fluctuations in Two-Dimensional Arrays of Small Josephson Junctions. *Phys. Rev. B* **1994**, *50*, 3959–3971.
13. Zolotavin, P.; Guyot-Sionnest, P. Meissner Effect in Colloidal Pb Nanoparticles. *ACS Nano* **2010**, *4*, 5599–5608.
14. Santhanam, V.; Liu, J.; Agarwal, R.; Andres, R. P. Self-Assembly of Uniform Monolayer Arrays of Nanoparticles. *Langmuir* **2003**, *19*, 7881–7887.
15. Klecha, E.; Ingert, D.; Pileni, M. P. How the Level of Ordering of 2D Nanocrystal Superlattices Is Controlled by Their Deposition Mode. *J. Phys. Chem. Lett.* **2010**, *1*, 1616–1622.
16. Luther, J. M.; Law, M.; Song, Q.; Perkins, C. L.; Beard, M. C.; Nozik, A. J. Structural, Optical, and Electrical Properties of Self-Assembled Films of PbSe Nanocrystals Treated with 1,2-Ethanedithiol. *ACS Nano* **2008**, *2*, 271–280.
17. Leatherdale, C. A.; Kagan, C. R.; Morgan, N. Y.; Empedocles, S. A.; Kastner, M. A.; Bawendi, M. G. Photoconductivity in Cdse Quantum Dot Solids. *Phys. Rev. B* **2000**, *62*, 2669–2680.
18. Dong, A.; Chen, J.; Oh, S. J.; Koh, W.-k.; Xiu, F.; Ye, X.; Ko, D.-K.; Wang, K. L.; Kagan, C. R.; Murray, C. B. Multiscale Periodic Assembly of Striped Nanocrystal Superlattice Films on a Liquid Surface. *Nano Lett.* **2011**, *11*, 841–846.
19. Bochenkov, V. E.; Zagorsky, V. V.; Sergeev, G. B. Cherairesistive Properties of Lead Nanoparticles, Covered by Oxide and Sulfide Layer. *Sens. Actuators, B* **2004**, *103*, 375–379.
20. Lide, D. R. *CRC Handbook of Chemistry and Physics: A Ready-Reference Book of Chemical and Physical Data*, 90th ed.; Lide, D. R., Ed.; CRC: Boca Raton, FL, **2009**.
21. George, S. M. Atomic Layer Deposition: An Overview. *Chem. Rev. (Washington, DC, U. S.)* **2010**, *110*, 111–131.
22. Buzea, C.; Yamashita, T. Structure Anisotropy of High-Temperature Superconductors: Resistance Peak Effect. *J. Optoelectron. Adv. Mater.* **2000**, *2*, 704–712.
23. Mrowka, F.; Manzoor, S.; Pongpiyapaiboon, P.; Maksimov, I. L.; Esquinazi, P.; Zimmer, K.; Lorenz, A. Excess Voltage in the Vicinity of the Superconducting Transition in Inhomogeneous $YBa_2Cu_3O_7$ Thin Films. *Phys. C (Amsterdam, Neth.)* **2003**, *399*, 22–42.
24. Mosqueira, J.; Pomar, A.; Diaz, A.; Veira, J. A.; Vidal, F. Resistivity Anomalies above the Superconducting Transition in $Y_1Ba_2Cu_3O_7$-Delta Crystals and Nonuniformly Distributed Critical-Temperature Inhomogeneities. *Phys. C (Amsterdam, Neth.)* **1994**, *225*, 34–44.
25. Collaboration: Authors and editors of the volumes III/17E-17F-41C: Lead Monoxide (PbO) Energy Gaps. Madelung, O., Rössler, U., Schulz, M., Eds.; SpringerMaterials—The Landolt-Börnstein Database (http://www.springermaterials.com) (accessed May 8, 2012).
26. Sheng, P.; Abeles, B. Voltage-Induced Tunneling Conduction in Granular Metals at Low Temperatures. *Phys. Rev. Lett.* **1972**, *28*, 34–37.
27. Collaboration: Authors and editors of the volumes III/17E-17F-41C: Lead Selenide (PbSe) Optical Properties, Dielectric Constant. Madelung, O., Rössler, U., Schulz, M. Eds.; SpringerMaterials—The Landolt-Börnstein Database (http://www.springermaterials.com) (accessed May 8, 2012).
28. Guyot-Sionnest, P. Electrical Transport in Colloidal Quantum Dot Films. *J. Phys. Chem. Lett.* **2012**, *3*, 1169–1175.
29. Tinkham, M. *Introduction to Superconductivity*, 2nd ed.; McGraw Hill: New York, 1996.
30. Zaccone, A.; Del Gado, E. On Mean Coordination and Structural Heterogeneity in Model Amorphous Solids. *J. Chem. Phys.* **2010**, *132*, 024906–024905.
31. Gantmakher, V. F.; Zverev, V. N.; Dolgopolov, V. T.; Shashkin, A. A. Pair Funneling in the Low-Temperature Conductivity of the Cd-Sb Alloy High-Resistance State near the Superconductor-Insulator Transition. *JETP Lett.* **1996**, *64*, 767–773.
32. Adkins, C. J.; Thomas, J. M. D.; Young, M. W. Increased Resistance below the Superconducting Transition in Granular Metals. *J. Phys. C: Solid State Phys.* **1980**, *13*, 3427–3438.
33. Shapira, Y.; Deutscher, G. Semiconductor-Superconductor Transition in Granular Al-Ge. *Phys. Rev. B* **1983**, *27*, 4463–4466.
34. Gerber, A.; Milner, A.; Deutscher, G.; Karpovsky, M.; Gladkikh, A. Insulator-Superconductor Transition in 3D Granular Al-Ge Films. *Phys. Rev. Lett.* **1997**, *78*, 4277–4280.
35. Lin, Y.-H.; Goldman, A. M. Hard Energy Gap in the Insulating Regime of Nominally Granular Films near the Superconductor-Insulator Transition. *Phys. Rev. B* **2010**, *82*, 214511.
36. Fistul, M. V.; Vinokur, V. M.; Baturina, T. I. Collective Cooper-Pair Transport in the Insulating State of Josephson-Junction Arrays". *Phys. Rev. Lett.* **2008**, *100*, 086805.
37. Efetov, K. B.; Feigel'man, M. V.; Wiegmann, P. B. Comment on "Collective Cooper-Pair Transport in the Insulating State of Josephson-Junction Arrays". *Phys. Rev. Lett.* **2009**, *102*, 049701.
38. Lopatin, A. V.; Vinokur, V. M. Hopping Transport in Granular Superconductors. *Phys. Rev. B* **2007**, *75*, 092201.
39. Abeles, B. Effect of Charging Energy on Superconductivity in Granular Metal Films. *Phys. Rev. B* **1977**, *15*, 2828–2829.
40. Fisher, M. P. A. Quantum Phase Transitions in Disordered Two-Dimensional Superconductors. *Phys. Rev. Lett.* **1990**, *65*, 923–926.
41. Schön, G.; Zaikin, A. D. Quantum Coherent Effects, Phase Transitions, and the Dissipative Dynamics of Ultra Small Tunnel Junctions. *Phys. Rep.* **1990**, *198*, 237–412.
42. Gerber, A. Low-Temperature Transport Properties of Granular Pb Films below the Percolation Threshold. *J. Phys.: Condens. Matter* **1990**, *2*, 8161.

43. Beloborodov, I. S.; Efetov, K. B. Negative Magnetoresistance of Granular Metals in a Strong Magnetic Field. *Phys. Rev. Lett.* **1999**, *82*, 3332–3335.
44. Beloborodov, I. S.; Efetov, K. B.; Larkin, A. I. Magnetoresistance of Granular Superconducting Metals in a Strong Magnetic Field. *Phys. Rev. B* **2000**, *61*, 9145–9161.
45. Glatz, A.; Varlamov, A. A.; Vinokur, V. M. Fluctuation Spectroscopy of Disordered Two-Dimensional Superconductors. *Phys. Rev. B* **2011**, 84.
46. Halperin, B. I.; Nelson, D. R. Resistive Transition in Superconducting Films. *J. Low Temp. Phys.* **1979**, *36*, 599–616.
47. Fiory, A. T.; Hebard, A. F.; Glaberson, W. I. Superconducting Phase Transitions in Indium/Indium-Oxide Thin-Film Composites. *Phys. Rev. B* **1983**, *28*, 5075–5087.
48. Ekin, J. W. Critical Currents in Granular Superconductors. *Phys. Rev. B* **1975**, *12*, 2676–2681.
49. Lobb, C. J.; Abraham, D. W.; Tinkham, M. Theoretical Interpretation of Resistive Transition Data from Arrays of Superconducting Weak Links. *Phys. Rev. B* **1983**, *27*, 150–157.
50. Goltsman, G. N.; Goghidze, I. G.; Kouminov, P. B.; Karasik, B. S.; Semenov, A. D.; Gershenzon, E. M. Influence of Grain-Boundary Weak Links on the Nonequilibrium Response of YBaCuO Thin-Films to Short Laser-Pulses. *J. Supercond.* **1994**, *7*, 751–755.